Renewable Energy 227 (2024) 120509

Contents lists available at ScienceDirect

Renewable Energy

journal homepage: www.elsevier.com/locate/renene

Wet torrefaction of biomass waste into high quality hydrochar and value-added liquid products using different zeolite catalysts

Andrii Kostyniuk [a,*], Blaž Likozar [a,b,c,d]

[a] Department of Catalysis and Chemical Reaction Engineering, National Institute of Chemistry, Hajdrihova 19, Ljubljana, 1001, Slovenia
[b] Faculty of Polymer Technology, Slovenj Gradec, 2380, Slovenia
[c] Pulp and Paper Institute, Bogišićeva 8, Ljubljana, 1000, Slovenia
[d] Faculty of Chemistry and Chemical Technology, University of Ljubljana, Večna pot 113, Ljubljana, 1000, Slovenia

ARTICLE INFO

Keywords:
Wet torrefaction
Biomass waste
Zeolites
Bio-ethanol and levulinic acid
Hydrochar

ABSTRACT

Wet torrefaction (WT) proves to be a highly efficient pretreatment method for biomass waste, resulting in the production of hydrochar and valuable liquid products. In this study, a groundbreaking chemocatalytic approach is introduced, employing various zeolite catalysts (H-ZSM-5, H-Beta, H–Y, H-USY, and H-Mordenite) in a batch reactor under a nitrogen atmosphere. This method enables the simultaneous one-pot production of levulinic acid (LA) and/or bio-ethanol during the WT process of wood cellulose pulp residue (WCPR), ultimately yielding high-quality solid fuel. The WT process involves at 220 and 260 °C, H_2O/WCPR = 10, and torrefaction time at 15, 30 and 60 min. The study identifies that at 220 °C and 15 min, as the optimal temperature and time, for bio-ethanol production, achieving a selectivity of 59.0 % with the H–Y catalyst, while the highest amount of bio-ethanol (75.6 %) was detected in presence of H-USY zeolite at 260 °C after 60 min. In addition, it was found the formation of relatively high amount of LA (62.0 %) at 220 °C after 60 min but using the H-ZSM-5 catalyst. For the WT + Mordenite sample (220 °C, 60 min), the highest carbon content of 71.5 % is achieved, resulting in the higher heating value (HHV) of 27.3 MJ/kg, an enhancement factor of 1.36, and carbon enrichment of 1.48, with the sequence of element removal during WT prioritized as DO > DH > DC and the weight loss of 68 %. Finally, the reaction mechanism was proposed to elucidate the formation of liquid products after WT of WCPR with participation of zeolite catalysts. The main pathway involving the direct conversion of cellulose into hydroxyacetone, followed by the subsequent generation of ethanol through the C–C cleavage of hydroxyacetone while LA formed via well-known route which includes cellulose hydrolysis to form glucose, conversion to 5-HMF and the subsequent transformation of 5-HMF into LA.

1. Introduction

The exhaustion of non-renewable fossil resources has precipitated global crises, manifesting as energy shortages and environmental deterioration. This is evidenced by widespread problems such as air pollution and global warming [1]. Amidst these challenges, there emerges a beacon of hope in the form of biomass, representing the singular wellspring of renewable carbon. This versatile resource holds immense promise for the conversion into invaluable biochemicals and biofuels, presenting a dual solution to the pressing dilemmas of energy scarcity and environmental degradation [2]. Biomass exhibits the remarkable capacity to undergo diverse thermochemical conversion technologies, yielding an array of solid, liquid, and gaseous biofuels [3]. These biofuels, in turn, emerge as a sustainable and eco-friendly alternative energy source. The intrinsic ability of biomass to serve as a raw material for these various conversion processes positions it as a pivotal player in the quest for cleaner and more sustainable energy solutions.

Various thermochemical technologies (such as torrefaction, pyrolysis, hydrothermal liquefaction, gasification, and combustion) stand at the forefront of harnessing the potential of biomass, transforming it into valuable energy resources [4]. Notably, torrefaction emerges as a significant green thermochemical process within this spectrum, facilitating the production of solid biofuel, commonly referred to as biochar or hydrochar, from diverse biomass resources, including woody and non-woody materials, forest residue, agricultural residue, agro-industrial waste, and municipal solid waste [5]. Hydrochar,

---

* Corresponding author.
E-mail address: andrii.kostyniuk@ki.si (A. Kostyniuk).

https://doi.org/10.1016/j.renene.2024.120509
Received 4 December 2023; Received in revised form 12 March 2024; Accepted 16 April 2024

distinguished by its versatile properties, finds application across a spectrum of uses, from greenhouse gas sequestration to serving as cost-effective adsorbents, enhancing soil, supporting catalysts, and more [6]. Torrefaction operates as a mild pyrolysis process aimed at several objectives, including enhancing higher heating values and energy densities, reducing atomic O/C and H/C ratios, lowering moisture content, improving water resistance, increasing grindability and reactivity, and achieving uniform properties [7]. Dry torrefaction (DT), executed in an oxygen-free environment with low heating rates, generally below 50 °C/min, takes place within a temperature range of 200–300 °C [8,9].

Conversely, wet torrefaction (WT), commonly recognized as hydrothermal torrefaction, represents a high-pressure thermal pretreatment process conducted in hot compressed water under inert conditions, typically at temperatures ranging from 180 to 260 °C for 15−60 min [10,11]. WT offers several advantages over DT, demanding notably lower temperatures and shorter holding times to achieve equivalent solid yields. This results in higher energy yields, a greater HHV, and improved hydrophobicity [12]. Consequently, WT proves to be a more effective method for biomass energy densification and conservation compared to DT.

Wood cellulose pulp residue (WCPR) stands as a pivotal element within the expansive pulp and paper sector, exerting considerable influence across diverse industries worldwide. Recent statistics from Statista [13] illustrate a steadfast output in the global pulp industry, surpassing 180 million metric tons annually for the past decade. In 2022, global wood pulp production surged to more than 195.79 million metric tons, representing a significant increase from the previous year and indicating a 15.5 % growth compared to the figures recorded in 2000. This sustained growth trajectory underscores the reliability and abundance of wood pulp as a primary resource, laying a solid foundation for the implementation of technologies like wet torrefaction on a larger scale. A steady supply of WCPR emerges as a linchpin for the successful integration of such processes, bolstering their feasibility and efficacy.

Zeolites, renowned for their acidity and porous structure, are chosen as catalysts for their ability to aid dehydration reactions and stimulate the production of targeted chemical compounds in WT [14,15]. The goal is to employ the catalytic properties of zeolite catalysts to improve the efficiency and selectivity of the WT process for WCPR. In this investigation, an innovative chemocatalytic method is proposed for the simultaneous one-pot generation of valued-added products (bio-ethanol and levulinic acid) from WCPR during WT conversion, employing H-ZSM-5, H-Beta, H–Y, H-USY, and H-Mordenite zeolite catalysts in a batch reactor under a nitrogen atmosphere to yield high-quality solid fuel. The experimental conditions involved maintaining a temperature of 220 °C for 15−60 min, with water serving as the reaction medium. Selecting 220 °C for WT aligns with earlier research, which identified this temperature as optimal in the absence of a catalyst. The primary objective was to optimize hydrochar production, striving for enhanced HHV and carbon content. Simultaneously, the aim was to yield valuable liquid products like ethanol and levulinic acid while unraveling the intricate mechanisms driving these transformations in presence of zeolite catalysts. Beyond these goals, a comprehensive analysis was conducted on both WCPR and the resultant hydrochar derived from the WT process. To achieve this, an array of characterization techniques was employed, encompassing X-ray diffraction (XRD), scanning electron microscopy (SEM), Brunauer-Emmett-Teller analysis (BET), elemental analysis (CHN(O)S), and thermogravimetric analysis (TGA). By conducting systematic experimentation and analysis, the objective was to clarify the function of zeolite catalysts in catalyzing biomass conversion reactions and enhancing the overall efficacy of WT.

2. Experimental section

The chemicals and materials used in this study are elaborated upon in section S1. Materials, which can be found in the Supplementary material. The feedstock, denoted as WCPR (wood cellulose pulp residue), was supplied by the biotechnology company Vertoro (Geleen, Netherlands). For a comprehensive breakdown of the composition of WCPR, please refer to Table S1.

2.1. Experimental apparatus and procedure

Wet torrefaction (WT) experiments on wood cellulose pulp residue (WCPR) were conducted in six stainless steel 75 mL (Parr) batch reactors, each equipped with online pressure and temperature control regulators, operating at 220 and 260 °C. The reaction mixture was stirred using a magnetic stirring bar with a stirring speed of 800 rpm. A precise amount (3.0 g) of WCPR was introduced into each reactor vessel. For the heterogeneously catalyzed reaction, 1.0 g of each zeolite catalyst was added into the reactor vessel. The electric heating temperature was controlled by the temperature program system, and the temperature inside the reactor was directly determined by an inline thermocouple. The initial reaction time started when the target reaction temperature was reached. After reaction, the autoclave was cooled rapidly in an ice bath. The solid catalyst and product solution were separated by filtration. Product solutions were collected through a 0.22 μm membrane filter. After separation, the collected hydrochars were dried at 105 °C overnight. The selection of 220 °C, coupled with durations of 15, 30, and 60 min, and a water/WCPR ratio of 10, was informed by previous research, which determined this temperature to be optimal for WT and the formation of high-value liquid products in the absence of a catalyst. The liquid samples collected underwent analysis using gas chromatography (GC) with an Agilent GC-7890A coupled with the Agilent 5977B GC/MSD, offering a measurement repeatability of the relative standard deviation (RSD) of ≤5 %. Hydrogen served as the carrier gas at a flow rate of 1 ml/min. Utilizing a capillary column of dimensions 30 m × 0.25 mm × 0.25 μm DB-WAX Ultra Inert, effective separation of products was achieved. Initially, the column was maintained at 40 °C for 4 min before ramping up the temperature to 200 °C at a rate of 12 °C/min, holding it there for 10 min. The split ratio was maintained at 1:150. Quantification of all products was conducted using an external calibration method that was verified.

2.2. Analysis

The structural characteristics of the H-ZSM-5, H-Beta, H–Y, H-USY, and H-Mordenite zeolite catalysts were determined through various methods, and the results are detailed in Table S2. Acid properties of the zeolite catalysts, assessed via temperature-programmed desorption of ammonia (NH_3−TPD), are presented in Table S3. NH_3 temperature-programmed desorption coupled with mass spectrometry (NH_3-TPD-MS) was conducted using a quartz U-tube reactor containing 0.1 g of catalyst [16]. The experiments were performed on an Autochem 2920 II instrument from the Micromeritics system, equipped with an online Pfeiffer Vacuum Thermostar quadrupole mass spectrometer. Initially, the catalyst underwent pretreatment in helium at 500 °C for 30 min [17]. Subsequently, NH_3 adsorption took place at 100 °C under a 10 vol % NH_3/He atmosphere, with a flow rate of 20 mL/min for 30 min. Following this, the samples were purged with helium at 100 °C for 60 min. Finally, the sample temperature was ramped up to 600 °C at a heating rate of 10 °C/min, and the NH_3-TPD profile was recorded. Simultaneously, NH_3 desorption ($m/z = 15$) was monitored during the NH_3-TPD-MS analysis. After completing the NH_3 desorption experiment, the mass spectrometer (MS) underwent calibration. This calibration involved subjecting the MS to at least five pulses of NH_3 at a known concentration. This calibration process was essential for quantifying the surface acidity of the selected catalysts [18]. Furthermore, pyridine adsorption diffuse-reflection infrared spectroscopy (Pyridine−DRIFTS) was conducted using a Frontier IR spectrometer from PerkinElmer, equipped with an MCT detector and the DiffusIR® accessory from Pike Scientific [19].

The textural properties of the WCPR and WT samples were evaluated using the N_2 adsorption-desorption method performed on a Micromeritics ASAP 2020 instrument. Prior to the experiment, a 150 mg sample was subjected to overnight degassing at 200 °C (ramping at 10 °C/min) under vacuum (10^{-3} Pa) [20]. Subsequently, N_2 adsorption-desorption analysis was conducted at −196 °C. The pore-size distribution was determined using the Barrett-Joyner-Halenda (BJH) method based on the desorption isotherms, while the total surface area was calculated using the Brunauer-Emmett-Teller (BET) method. Additionally, the FE-SEM SUPRA 35-VP instrument from Carl Zeiss facilitated high-resolution scanning electron microscopy (HR-SEM) inspection of WCPR and wet torrefied WCPR samples. X-ray diffraction (XRD) analysis utilized the PANalytical XpertPro powder X-ray diffraction instrument, employing CuKα1 radiation at 45 kV and 40 mA. The scanning range spanned from 5 to 50° with increments of 0.033°. To determine carbon, hydrogen, nitrogen, and sulfur levels, the vario EL cube elemental analyzer from Elementar in Hanau, Germany, operated in CHNS mode. Detection was achieved using a thermal conductivity detector for carbon, hydrogen, and nitrogen, while an infrared detector measured sulfur. Calibration involved utilizing a low-level standard from Elementar, containing 67.65 % carbon, 4.95 % hydrogen, 0.72 % nitrogen, and 0.84 % sulfur. The combustion tube was heated to 1150 °C, and the reduction tube to 850 °C. The assessment of CHNOS content was performed on a dry basis after subtracting the water content.

$$O = 100\% - C\% - H\% - N\% - S\% - moisture\% - A\% - Si\% - Al\% \quad (1)$$

Utilizing a TGA-IR (thermogravimetric analysis-infrared spectrometry) Spectrum 3 with EGA 4000 from PerkinElmer, the pyrolysis of dried and torrefied cellulose was investigated. Each test used approximately 10 mg of sample, and the temperature was raised from 40 to 750 °C at a heating rate of 10 °C/min. A high-purity carrier gas of nitrogen (>99.999 %) was employed, flowing at a rate of 20 mL/min. The experimental results obtained from TGA were automatically captured by a computer.

Proximate analysis was conducted to determine the moisture, volatile matter, fixed carbon, and ash content in both untreated and wet torrefied WCPR, utilizing a thermal gravimetric analyzer—specifically, the Spectrum 3 with EGA 4000 by PerkinElmer. Moisture content, ash content, and volatile matter were assessed according to the standards set forth by the American Society for Testing and Materials (ASTM): E−871 for moisture, E−1755 for ash, and E−872 for volatile matter [21–23]. In this analytical procedure, around 10 mg of the sample underwent controlled heating within a nitrogen atmosphere. The process commenced at 40 °C and progressed to 120 °C, with a 10 min interval to measure the moisture content (MC, %). Following this, a heating rate of 50 °C/min was applied until reaching 800 °C, and a 20 min hold was introduced to determine the volatile matter (VM, %). For the determination of ash content (Ash, %), the cooling phase was initiated with a cooling rate of −50 °C/min until reaching 450 °C. At this point, the nitrogen atmosphere was replaced with air, and a new heating ramp of 25 °C/min ensued, continuing until 800 °C, and then maintaining isothermally for 3 min. The fixed carbon content (FC, %) was calculated using Equation (2).

$$FC = 100 - (MC + Ash + VM). \quad (2)$$

Equation (3) was utilized to calculate the HHV for both the WCPR and the WT + Zeolite samples [24,25].

$$HHV\ (MJ/kg) = 0.3491 \times C + 1.1783 \times H - 0.1034 \times O + 0.1005 \times S - 0.0151 \times N - 0.0211 \times A \quad (3)$$

In this expression, C, H, O, S, N, and A denote the carbon, hydrogen, oxygen, sulfur, nitrogen, and ash contents, respectively, derived from elemental analysis and expressed as weight percentages on a dry basis. The utilization of these equations allows for the computation of both the higher and lower heating values of the biomass, providing a comprehensive understanding of its energy properties under torrefaction conditions. The formulas applied to determine the solid yield and energy yield of the torrefied samples were as follows:

$$Y_{solid} = \left(m_{poduct} \middle/ m_{feedstock}\right) \times 100\% \quad (4)$$

$$Y_{energy} = \left(\left(Y_{solid} \times HHV_{product}\right) \middle/ HHV_{feedstock}\right) \times 100\% \quad (5)$$

where Y_{solid} – the solid yield, and Y_{energy} – the energy yield. The variables $m_{feedstock}$ and $m_{product}$ means the mass of the initial samples and the solid product following WT, respectively. $HHV_{feedstock}$ and $HHV_{product}$ denote the higher heating value (in MJ/kg) of the initial samples and the solid product after WT, respectively [26].

Decarbonization (DC), dehydrogenation (DH), and deoxygenation (DO) are three metrics used to measure the reduction in the mass of carbon, hydrogen, and oxygen during biomass torrefaction [27]. DC quantifies the percentage of carbon loss in the biomass due to WT and can be determined using the following equation:

$$DC\ (\%) = 100 - Y_{solid}\ (\%) \times \left(C_{product} \middle/ C_{feedstock}\right) \quad (6)$$

DH and DO can be similarly calculated using the same procedure as DC.

$$DH\ (\%) = 100 - Y_{solid}\ (\%) \times \left(H_{product} \middle/ H_{feedstock}\right) \quad (7)$$

$$DO\ (\%) = 100 - Y_{solid}\ (\%) \times \left(O_{product} \middle/ O_{feedstock}\right) \quad (8)$$

where $O_{product}$ and $O_{feedstock}$ are the dry ash free oxygen content of the WT + Zeolite and WCPR samples, respectively.

A metric known as carbon enrichment (CE), employed to evaluate the extent of carbonization in WT + Zeolite samples, is defined as follows:

$$CE = C_{product}/C_{feedstock} \quad (9)$$

The weight loss (WL) of WT + Zeolite samples is expressed as follows:

$$WL\ (\%) = 100 - Y_{solid} \quad (10)$$

The enhancement factor (EF) was defined as follows [27]:

$$EF = HHV_{product}/HHV_{feedstock} \quad (11)$$

Carbon yield (Y_C) and hydrogen yield (Y_H) were calculated as follow:

$$Y_C\ (\%) = Y_{solid}\ (\%) \times \left(C_{product} \middle/ C_{feedstock}\right) \quad (12)$$

$$Y_H\ (\%) = Y_{solid}\ (\%) \times \left(H_{product} \middle/ H_{feedstock}\right) \quad (13)$$

where $C_{product}$, $H_{product}$ and $C_{feedstock}$, $H_{feedstock}$ are the dry ash free carbon and hydrogen content of the WT + Zeolite and WCPR samples, respectively.

3. Results and discussion

3.1. XRD analysis of WCPR and WT + Zeolite samples

The X-ray diffraction (XRD) patterns obtained for both the WCPR and the corresponding WT + Zeolite samples are presented in Fig. 1. The XRD spectra for WCPR revealed distinct peaks at 2θ values of 15.6, 22.4, and 34.4°. These peaks were identified as the crystalline planes indexed as (110), (200), and (004), respectively, within the cellulose type I allomorph's crystal structure. It is essential to highlight that cellulose is the only component exhibiting a crystalline structure, whereas hemicellulose and lignin display amorphous characteristics [28]. It was found a significant alteration in the crystalline integrity of cellulose during the WT process. This transformation includes modifications in the polymorphic structure of cellulose I, resulting in a noticeable decrease in its crystallinity and the significant decrease and/or disappearance of

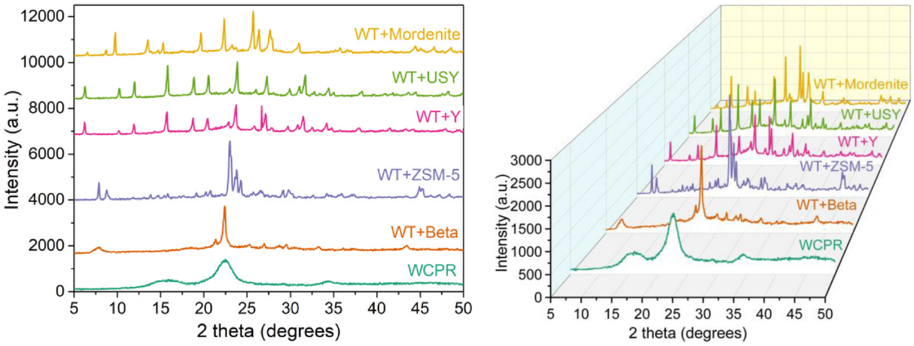

Fig. 1. X-ray diffraction patterns of the WT + Zeolite samples at 220 °C as compared to the raw material – WCPR.

characteristic peaks. The XRD pattern of the WT + Zeolite samples with the presence of zeolites, associated with the XRD patterns of the H-Beta, H-Mordenite, H–Y, H-USY, and H-ZSM-5 catalysts. It can be seen that different WT + Zeolite produce different XRD patterns corresponding to BEA, MOR, FAU, and MFI zeolite structure, respectively [19]. The high degree of crystallinity with strong intensity diffraction peaks was observed in 2 theta region 20−25° (Fig. 1) at 23.1, 23.3, 23.7, 23.9, 24.4° for the H-ZSM-5 and H-USY zeolites. In the case of the H-Beta, H-Mordenite, H–Y zeolites the most intensive peaks are located in the 2 theta region at 20.4, 22.4, 23.3, 23.7°. In addition, the small-angle X-ray diffraction peaks exhibited high intensity for the H- ZSM-5 catalyst at 7.9, 8.8 and 9.1° and the H-USY at 6.3°, while the H-Beta, H-Mordenite, H–Y at 6.2, 6.5, 7.8, 8.7, and 9.8°.

3.2. *Elemental components and surface properties of WCPR and WT + Zeolite samples*

Table S4 presents proximate analysis data, providing valuable insights into the compositional transformations of WCPR during the WT process in the presence of H-ZSM-5, H-Beta, H–Y, H-USY, and H-Mordenite zeolite catalysts. Notably, the volatile matter content experiences a significant reduction compared to the raw feedstock. Starting at 75.5 % for WCPR, it consistently decreases to 29.5 % for the WT + Beta sample. Meanwhile, the fixed carbon content demonstrates a distinct trend during WT, rising from 19.8 % for untreated WCPR to 32.7 % for the WT + USY sample (Table S4). The slightly lower fixed carbon content (27.9 %) observed in the hydrochar produced using the Y zeolite catalyst compared to hydrochar produced using other catalysts (29.5–32.7 %) can be attributed to the higher surface area of zeolite Y. During the WT of WCPR, the higher surface area of zeolite Y facilitates the deposition of more carbonaceous species. This leads to a higher proportion of volatile matter and a lower fixed carbon content in the resulting hydrochar.

Additionally, the WT sample without a catalyst (WT_WCPR_220) was investigated under identical reaction conditions, revealing a fixed carbon content of 21.3 %. This value is considerably lower than that observed in all the examined WT + Zeolite samples. The cumulative percentage of ash, silicon, and aluminum (Ash + Si + Al) unveils intriguing patterns in residue/mineral composition. Initiating at 3.2 % for WCPR, this combined percentage experiences a substantial increase with the addition of zeolites, culminating at 36.4 % for the WT + ZSM-5 sample.

This escalation can be attributed to a concentration effect, wherein volatile components are released, leading to an augmented formation of coke and, consequently, a higher proportion of ash. Additionally, the substantial presence of silicon and aluminum from the zeolite contributes significantly to this observed rise.

The elemental analysis data presented in Table S4 and Fig. 3b offer a quantitative insight into the compositional variations in WCPR during hydrothermal upgrading with different types of zeolites at 220 °C. Beginning with WCPR, the carbon content undergoes a substantial increase from 48.3 % to 72.6 % in the WT + ZSM-5 sample, signifying a noteworthy enrichment in carbonaceous material. In contrast, the hydrogen content experiences a decrease, dropping from 6.2 % in the WCPR feedstock to 3.1 % in the WT + ZSM-5 case. Moreover, WCPR, initially possessing an oxygen content of 40.3 %, sees a reduction to 15.9 % in the WT + Mordenite sample. This decline aligns with the removal of oxygenated functional groups, indicating the transformation of biomass waste and an enhancement in fuel properties. Notably, nitrogen and sulfur levels remain minimal across all samples.

The structural and morphological characteristics of the investigated samples are detailed in Table S4. The parameters under scrutiny encompass temperature, BET surface area (m^2/g), and average pore diameter (PD, nm). The BET surface area serves as a pivotal factor influencing the adsorption and catalytic properties of materials. Notably, the WT + Y sample displays the highest BET surface area (80.6 m^2/g) among the samples, indicating a substantial availability of surface area for catalytic activities (Fig. 2a). In contrast, the WCPR feedstock and WT_WCPR_220 exhibit the lowest surface areas, measuring 3.4 and 3.5 m^2/g, respectively, suggesting notable differences in porous structure compared to the WT + Zeolite samples. The hydrochar produced at WT + Y exhibited the maximum BET surface area primarily due to the characteristics of the pristine zeolite catalysts. It is shown (Table S2) that H–Y and H-USY catalysts possess notably higher surface areas (665–667 m^2/g) compared to other zeolite catalysts such as H-ZSM-5 (348 m^2/g), H-Mordenite (418 m^2/g), and H-Beta (549 m^2/g). Consequently, during the WT process, both WT + Y and WT + USY retained a higher BET surface area (80.6 and 38.4 m^2/g, respectively) in comparison to WT + ZSM-5, WT + Mordenite, and WT + Beta, which exhibited surface areas of 24.6, 22.8, and 22.7 m^2/g, respectively. This difference underscores the significant influence of the initial zeolite catalyst's surface characteristics on the resulting hydrochar's BET surface area during the WT process. The average pore diameter, determined by the BJH method, provides insights into the pore size distribution. The WCPR feedstock features a relatively larger average pore diameter (39.4 nm) compared to the smallest pore diameter observed in the WT + Y sample (14.7 nm). This difference in pore diameter may impact the diffusion and accessibility of reactants within the materials, thereby influencing their catalytic performance. Notably, the WT + Y sample stands out with the highest ethanol yield (60 %) at 220 °C after 60 min (Fig. 7a). This exceptional performance aligns with both the greatest surface area and the smallest pore diameter when compared to the other samples studied.

In Fig. 2b, the weight loss (WL) observed across all WT samples utilizing zeolite catalysts consistently fell within the range of 65.0–69.5 %. It's important to note that the differences in WL between these samples were generally marginal, typically less than 5 %. Specifically, the WT + Y sample exhibiting a WL of 65.0 % represents one such minor variation. These slight differences in WL can be attributed to several factors, including variances in catalyst acidity, morphology, and texture. These characteristics play a significant role in determining the quantity of liquid byproducts generated during the hydrochar production

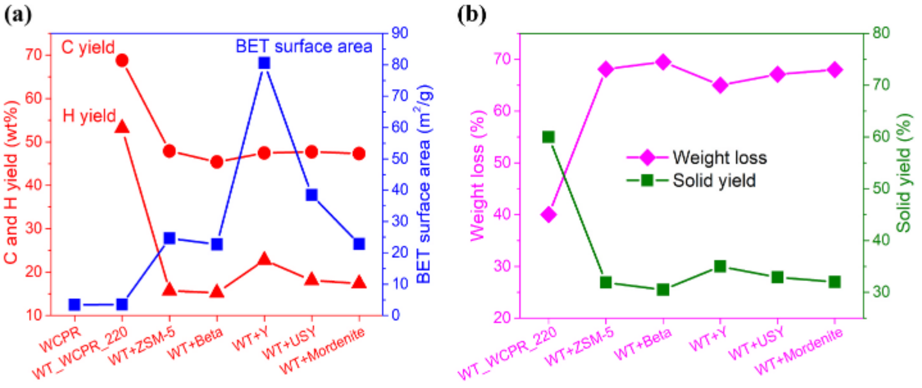

Fig. 2. (a) – profiles of C and H yield and BET surface area and (b) – weight loss and solid yield of WCPR, WT_WCPR_220, and WT + Zeolite samples at 220 °C.

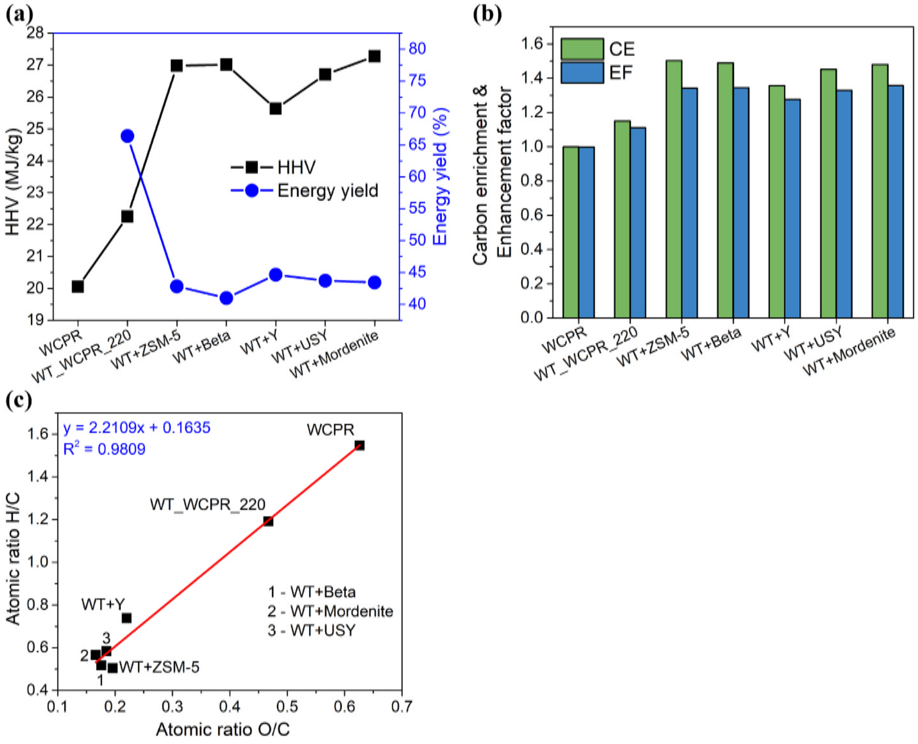

Fig. 3. HHV and energy yield – (a) and carbon enrichment (CE) and enhancement factor (EF) – (b) and H/C versus O/C ratio in terms of atomic basis (van Krevelen diagram) – (c) for WCPR, WT_WCPR_220, and WT + Zeolite samples at 220 °C.

process, thereby influencing WL. Hence, while there may be subtle discrepancies in WL among the samples, these variations are not considered substantial and can be attributed to the intrinsic properties of the catalysts utilized. In stark contrast, the WT_WCPR_220 sample exhibits a significantly lower weight loss, around 40 %, indicating a higher formation of liquid products when zeolite catalysts are employed in the hydrothermal upgrading (WT) process.

Conversely, concerning solid yield, there is a reverse scenario, with the WT_WCPR_220 sample showing the highest value (60 %), while the WT + Zeolites exhibit values in the range of 30.5–35.0 %. This decrease in solid yield is attributed to the greater involvement of chemical reactions during hydrothermal upgrading in the presence of catalysts [27].

3.3. HHV, solid, carbon, hydrogen, energy yields, DC, DH, DO, enhancement factor, carbon enrichment, weight loss and atomic ratios of O/C and H/C of WCPR and WT + Zeolite samples

This chapter focuses on evaluating the HHVs associated with untreated WCPR, WT_WCPR_220, and WT + Zeolite samples. The HHVs of the WT + Zeolite samples exhibit an increasing trend, underscoring the significance of temperature and the presence of catalyst in influencing the energy content of the resulting hydrochar (Table S5). The HHV of WCPR (20.1 MJ/kg) is surpassed by all WT + Zeolite samples, with the WT + Mordenite sample displaying the highest HHV (27.3 MJ/kg) at 220 °C after 60 min. Furthermore, a comparison was made with the HHVs of the WT_WCPR_220 sample (Fig. 3a). The WT_WCPR_220 sample exhibits an HHV of 22.3 MJ/kg, which is lower than all WT + Zeolite samples, with HHVs ranging from 25.6 to 27.3 MJ/kg. This comparison highlights the favorable impact of zeolite catalysts on enhancing the higher heating values of the hydrochar produced during the hydrothermal upgrading process. The WT + Mordenite sample exhibited the highest HHV due to the exceptional properties of H-Mordenite zeolite, particularly its high acidity. It is found (Table S3) that H-Mordenite possesses a notably higher total acidity (4.69 mmol$_{NH3}$/g$_{cat}$) compared to other zeolite catalysts such as H-Beta, H-ZSM-5, H–Y, and H-USY, which have much lower total acidity ranging from 1.75 to 2.08

$mmol_{NH3}/g_{cat}$ [19,29]. The acidity of the catalyst plays a crucial role in altering the structure and physical and chemical properties of hydrochars and their ashes [30]. The presence of acidic catalysts significantly influences the WT process, leading to the production of hydrochars with higher HHV [31]. Acidic catalysts facilitate the removal of water molecules from biomass during the WT process and promote the breakdown of complex organic compounds into simpler ones. Additionally, under acidic conditions, organic matter is more efficiently converted into carbonaceous material, contributing to the higher HHV observed in the WT + Mordenite sample.

Energy yield serves as a quantitative metric for assessing the efficiency of a system or process, reflecting the percentage of energy extracted or generated relative to the total available energy in the input material. In this study, the hydrochar with the highest energy yield was observed in the WT + Y sample, despite the energy yields across all WT + Zeolite samples falling within a relatively narrow range of 41.0–44.6 %. Specifically, the WT + Y sample exhibited the highest energy yield at 44.6 %, while the lowest energy yield, 41.0 %, was recorded in the WT + Beta sample. The difference of less than 4 % highlights the subtle variations among the samples. Several factors contribute to these differences in energy yield, including variations in zeolite acidity, morphology, texture, structure, and composition. Notably, a comparison with the WT_WCPR_220 sample revealed an energy yield of approximately 66.4 %, showcasing a substantial increase.

Table S5 and Fig. 2a provide carbon and hydrogen yield data, indicating a carbon yield in the range of 45.4–47.9 % and a corresponding hydrogen yield ranging from 15.3 to 22.8 %. This observation suggests that, with the exception of the WT + Y sample, there is no significant difference among the studied samples in terms of carbon yield. However, the WT + Y sample showed a higher hydrogen yield (22.8 %) compared to the other WT samples with catalysts present. The difference in hydrogen yield observed in the WT + Y sample compared to the other samples in the study can be attributed to several standout properties of the H–Y catalyst. These properties play a crucial role in influencing hydrogen yield and enhancing the efficiency of biomass conversion processes. Firstly, the acidity of H–Y zeolite is a key factor contributing to the high hydrogen yield. H–Y zeolite tends to possess an optimal level of acidity, striking the right balance that facilitates the breakdown of WCPR compounds into hydrogen-rich compounds. This acidity initiates and promotes the desired reactions that lead to increased hydrogen yield. Furthermore, the pore structure of H–Y zeolite is highly conducive to efficient catalytic processes. Its intricate network of pores and channels provides ample surface area for reactant molecules to interact, facilitating enhanced conversion of WCPR into hydrogen-rich compounds. This optimized pore structure promotes better accessibility of reactants to active sites within the catalyst, thereby improving overall conversion efficiency. Moreover, the stability of H–Y catalyst, both thermally and hydrothermally, ensures continuous and consistent hydrogen-rich compounds even under harsh operating conditions. This stability allows the catalyst to maintain its effectiveness over prolonged periods, sustaining high hydrogen yields over time. In essence, the combination of optimal acidity, pore structure, catalytic activity, and stability makes H–Y catalysts highly efficient in promoting hydrogen-rich compounds from biomass sources like WCPR. When these factors work together synergistically, as observed in the WT + Y sample, they create an ideal environment for maximizing hydrogen yield. At the same time, the WT_WCPR_220 sample, without the presence of zeolites, demonstrated the highest hydrogen yield (53.2 %) and carbon yield (68.8 %) among all samples tested.

In Fig. 3b, the enhancement factors show a significant increase when catalysts are employed for WT + Zeolite, ranging from 1.28 to 1.36, compared to WCPR (1.00) and WT_WCPR_220 (1.11) samples. Correspondingly, carbon enrichment values also demonstrate an increase from 1.00 to the 1.36−1.50 range for the WT + Zeolite samples, while the WT_WCPR_220 sample achieved an enrichment factor of only 1.15. These findings underscore the positive impact of catalysts in enhancing both energy yield and carbon enrichment during the hydrothermal upgrading process.

The van Krevelen diagram, as illustrated in Fig. 3c, presents the atomic ratios of H/C and O/C. This graphical representation reveals a notable linear relationship ($R^2 = 0.9809$), demonstrating that both H/C and O/C ratios decline as temperature increases (up to 220 °C) and zeolite catalysts are introduced under an N_2 atmosphere. The decrease in H/C and O/C ratios observed in the van Krevelen diagram indicates an augmented carbonization process [32]. This reduction suggests an enhancement in carbonization efficiency with the addition of zeolite catalysts and the elevation of temperatures, underscoring a significant correlation between catalyst presence, temperature, and carbonization efficacy.

Table S5 and Fig. 4 provide comprehensive data on decarbonization (DC), dehydrogenation (DH), and deoxygenation (DO), encompassing elemental analysis of WCPR, WT_WCPR_220, and WT + Zeolite samples at 220 °C after 60 min. The elemental removal sequence during WT, with DO > DH > DC, underscores the substantial impact of WT on reducing oxygen content compared to other elements [33]. The WT_WCPR_220 sample exhibits lower performance indicators with DO (43.2 %) > DH (41.1 %) > DC (31.2 %) in terms of elemental removal. Conversely, the WT + Beta sample demonstrates the highest indices with DO (82.8 %) > DH (79.5 %) > DC (54.6 %). However, it’s important to emphasize that these differences are marginal, typically within a 1–2% range. It is evident that WT has a more significant impact on oxygen and hydrogen removal than on carbon. This discrepancy can be attributed to the release of moisture and light volatiles during the WT process, facilitated through mechanisms such as dehydration, dehydroxylation, devolatilization, and decomposition of WCPR [27].

3.4. TG analysis of WCPR and WT + Zeolite samples

Thermogravimetric analysis (TG) was conducted on both WCPR and WT + Zeolite samples in a nitrogen environment, offering valuable insights into their pyrolysis behavior under various temperature conditions (Fig. 5). These insights significantly contribute to a comprehensive understanding of the thermal stability and decomposition characteristics inherent in these materials. In order to explore the thermal degradation and combustion behaviors, a temperature range from 50 to 750 °C was investigated. Specifically, samples were analyzed at 220 °C with WT durations of 15, 30, and 60 min. The selection of 220 °C for the WT aligns with prior research, which identified it as the optimal temperature in the absence of a catalyst.

In the TG curves, the residual mass demonstrated an increasing trend following WT at 220 °C using zeolite catalysts, elevating from 21.2 % for WCPR and WT_WCPR_220 (Fig. 5b) to 61−66 % after 15 min, 45−66 % after 30 min, and 56−67 % after 60 min. Remarkably, the residual masses of WT + ZSM-5 (64.9 %), WT + Beta (65.5 %), WT + Y (45.0 %), WT + USY (65.1 %), and WT + Mordenite (62.6 %) were 3.06, 3.09, 2.12, 3.07, and 2.95 times higher than that of the WCPR and WT_WCPR_220 samples, respectively. This finding suggests an enhancement in thermal stability with WT pretreatment in the presence of a catalyst. TG analysis revealed that WCPR and WT_WCPR_220 samples experienced the highest weight loss within the temperature range of 275–350 °C. In contrast, all WT + Zeolite samples displayed high thermal stability, with the exception of the WT + Y sample, which exhibited the highest weight loss but still lower than that of the WCPR and WT_WCPR_220 samples. Notably, despite its slightly lower thermal stability, the WT + Y sample produced the highest yield of bio-ethanol.

3.5. HR SEM analysis of WCPR and WT + Zeolite samples

The SEM images in Fig. 6 highlight significant disparities among the WCPR raw material, WT_WCPR_220, and WT + Beta samples. Following WT, the hydrochar displayed a smooth surface morphology compared to the untreated WCPR feedstock (Fig. 6a and b). While WCPR exhibited a

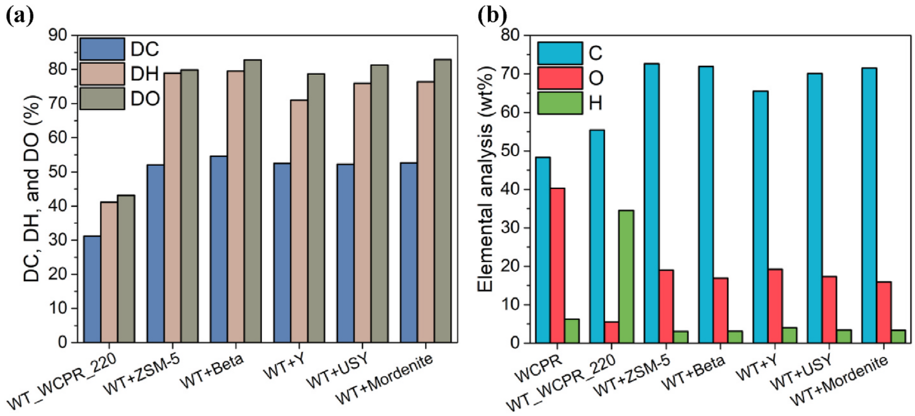

Fig. 4. (a) – Profiles of decarbonization (DC), dehydrogenfation (DH), and deoxygenation (DO) and (b) – elemental analysis (C, O, H) of WCPR, WT_WCPR_220, and WT + Zeolite samples at 220 °C.

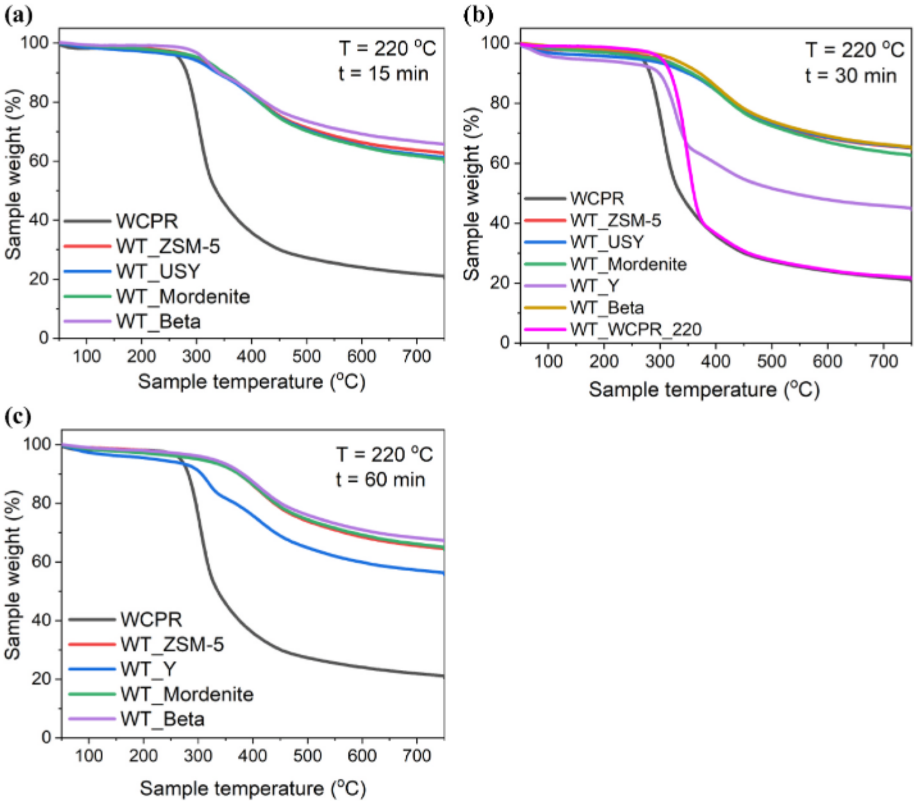

Fig. 5. TG curves for WCPR, WT_WCPR_220 (30), and WT + Zeolite samples with 1.0 g of zeolite within 15 – (a), 30 – (b) and 60 min – (c) at 220 °C at the heating rate of 10 °C/min in nitrogen atmosphere.

typical porous structure of untreated biomass materials, the cellulose surface underwent a transformative process after wet torrefaction in the presence of H-Beta zeolite (Fig. 6c). This process resulted in a smoother texture with some grooves, retaining elements of the original fiber morphology. This change is attributed to thermochemical and catalytic reactions during the WT process. Surface area and pore characteristics, detailed in Table S4, show an increase in the hydrochar's surface area post-wet torrefaction, albeit with a reduction in pore diameter. Additionally, H-Beta zeolite particles were observed on the hydrochar (Fig. 6c), indicating its role in facilitating the WT process by promoting intermediates' formation and catalyzing specific reactions, leading to the production of valuable products such as ethanol or LA.

Furthermore, these differences were analyzed through SEM-EDX elemental composition data (Table S6). In the WCPR sample, the main elements detected were C and O, which are characteristic components of cellulose. The carbon content ranged from 57.97 % to 58.57 %, while the oxygen content ranged from 41.69 % to 41.85 %. WT of WCPR at 220 °C for 30 min (referred to as WT_WCPR_220) resulted in shifts in the elemental composition of cellulose. There was a slight increase in carbon content compared to the WCPR feedstock, ranging from 58.75 % to 59.42 %, while the oxygen content exhibited a decrease, ranging from 40.58 % to 41.25 %. Upon WT with the H-Beta catalyst at 220 °C for 30 min, significant changes in the elemental composition were observed. The carbon content decreased substantially, ranging from 45.15 % to 46.57 %, while the oxygen content increased, ranging from 43.72 % to 45.45 %. Notably, Si was detected in relatively high amounts, ranging from 8.23 % to 8.90 %, along with Al present at levels of 0.69 %–0.73 %. The appearance of Si and Al suggests that the H-Beta catalyst became

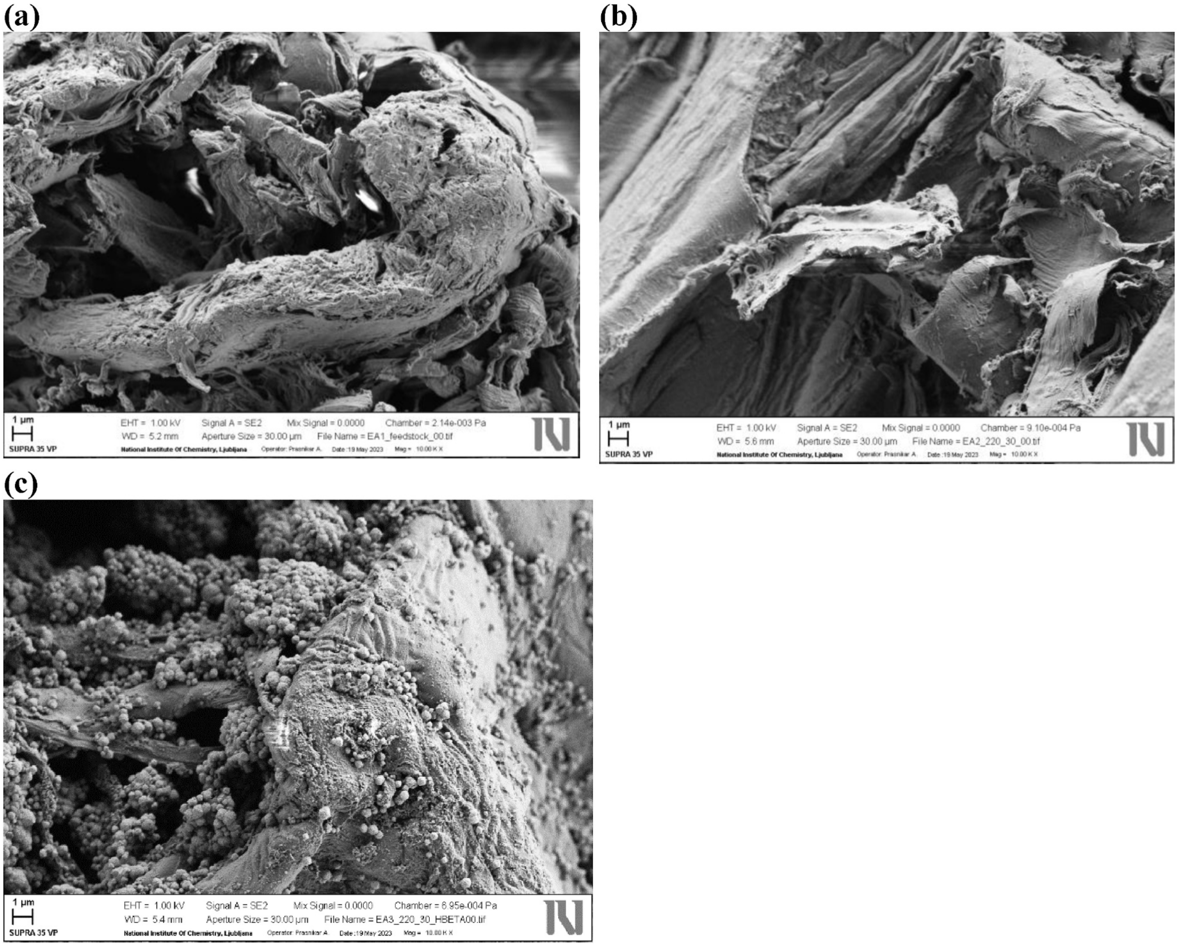

Fig. 6. SEM scans of WCPR – (a), WT_WCPR_220_30 − (b) and WT + Beta samples at 220 °C after 30 min − (c).

incorporated into the torrefied sample, likely due to interactions during the WT process.

Thus, the observed changes in carbon and oxygen content can be attributed to the thermochemical reactions that occurred during the WT process. As the torrefaction temperature and time increased, the cellulose underwent significant transformations, leading to the breakdown of carbon-rich cellulose molecules and the release of volatile components. These reactions resulted in the conversion of cellulose into other products, such as ethanol, LA and other degradation byproducts.

To enrich the discussion and enhance the comparison with the results of other researchers, a thorough data analysis was conducted. The results are depicted in Table S7, which provides a comparison of the HHV and elemental composition of biochar derived from diverse biomass types after undergoing WT under ideal reaction conditions. Table S7 underscores that the WT + Mordenite sample exhibits the highest HHV (27.3 MJ/kg) and carbon content (71.5 wt%) in biochar compared to a variety of biomass materials, such as bamboo sawdust [34,35], rice husk [36], corn stalk [37], beech [38], wheat straw [38,39], spruce [40], birch [40], oil trimmings and pulp [41], eucalyptus bark [42], palm oil empty fruit bunches [43], grape pomace [44], and dried olive pomace [45]. Across all considered biomass types, there is a consistent rise in HHV with increasing temperature, with HHV strongly correlating with the carbon, hydrogen, oxygen, and nitrogen content of the biomass. Despite the WT temperature not being the highest compared to most studies (Table S7), where temperatures ranged from 230 to 350 °C, the HHV and carbon content exceed literature data, while maintaining the lowest oxygen content (15.9 wt%). This improvement in HHV of wet torrefied WCPR is attributed to the increased carbon content and reduced oxygen content resulting from more pronounced dehydration reactions facilitated by the H-Mordenite catalyst compared to biomass sources from literature where the catalyst was absent. Additionally, it is proposed that the decrease in oxygen content primarily stems from the degradation of cellulose due to its interaction with the highly acidic H-Mordenite zeolite catalyst [30].

3.6. Effect of process parameters on the liquid product distribution of WT + Zeolite samples

3.6.1. Effect of reaction time and temperature on the product distribution in the liquid phase of WT + Zeolite samples

Fig. 7 presents the results of a study on the effect of reaction time on the WT of WCPR with the addition of various zeolite catalysts at 220 °C. The primary focus of the study revolves around the distribution of products in the liquid phase, specifically the conversion of cellulose into different chemical compounds such as ethanol (EtOH), levulinic acid (LA), formic acid (FA), 5-hydroxymethylfurfural (5-HMF), furfural (FUR), etc. The data reveals a discernible pattern: the formation of ethanol tends to decrease with shorter reaction times, while there is an observed increase in the production of LA with prolonged reaction times. This trend suggests that ethanol is an early product, reaching its highest concentration of 59.0 % after just 15 min at 220 °C for the WT + Y sample. Conversely, after a 60 min duration at 220 °C, LA emerges as the primary product, achieving the highest selectivity recorded at 62.0 % for the WT + ZSM-5 sample. The primary reason for the elevated ethanol yield in the WT + Y sample is believed to be the optimal balance achieved by the H–Y catalyst in terms of acidity, pore diameter, and surface area. The H–Y catalyst possesses specific properties that contribute to its effectiveness in promoting ethanol yield. Notably, the

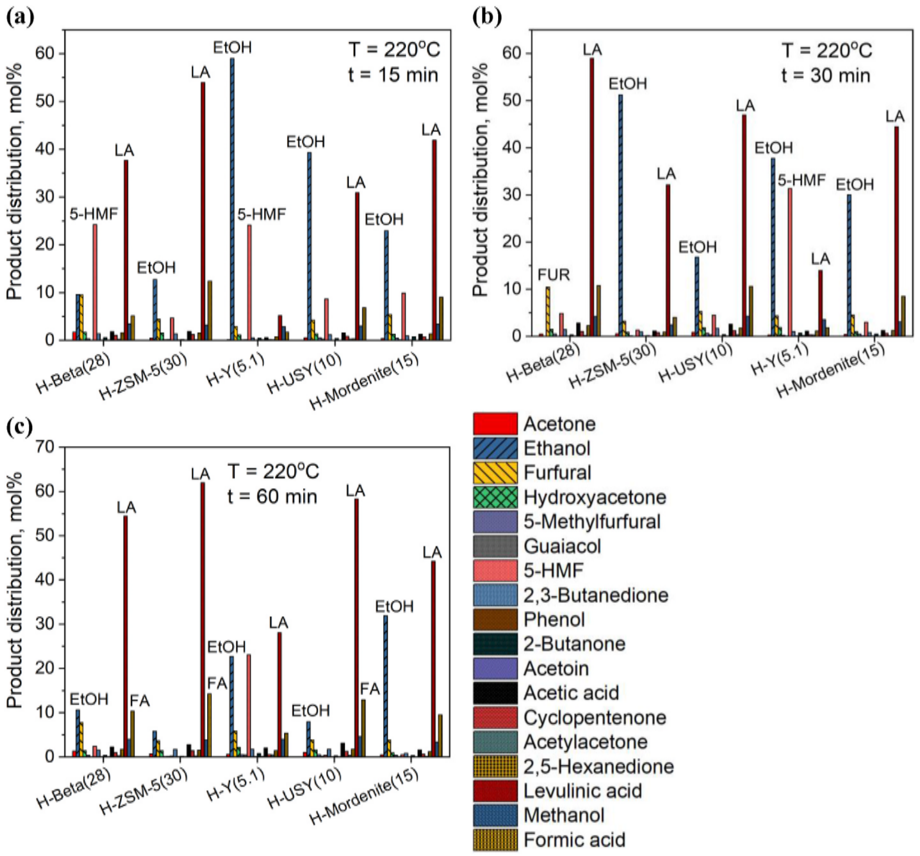

Fig. 7. Effect of reaction time (a – 15 min, b – 30 min, c – 60 min) on liquid-phase product distribution for the WT + Zeolite samples. Reaction conditions: 3.0 g of WCPR, 30 mL of water, 1.0 g of H-Beta, H-ZSM-5, H–Y, H-USY or H-Mordenite catalysts, stirring speed at 900 rpm, T = 220 °C.

acidity of the H–Y catalyst is likely well-suited for the conversion of the WCPR to ethanol. Additionally, the pore diameter of the catalyst may facilitate the diffusion of reactants and products, promoting efficient conversion processes. Furthermore, the high surface area of the H–Y catalyst among the tested samples could provide more active sites for ethanol production (Table S2 and Table S4).

Interestingly, when the WT temperature was increased to 260 °C (Fig. 8), the liquid product distribution significantly changed and varied for different catalysts. For instance, the WT + Y and WT + USY samples featured ethanol as the main liquid product, with the highest amount (75.6 %) for the WT + USY sample, while the ethanol content decreased to 57.8 % for WT + Y. This can be explained by the different catalytic activities and stabilities of H–Y and H-USY zeolites at elevated reaction temperatures. The significant ethanol production observed in the WT + USY sample (at 260 °C after 60 min) is attributed primarily to the exceptional stability of the H-USY catalyst compared to the H–Y zeolite. The H-USY catalyst possesses several outstanding properties that likely contribute to its ability to yield high amounts of ethanol. Firstly, the high surface area of the H-USY catalyst provides ample active sites for catalytic reactions, thereby facilitating the conversion of the WCPR feedstock into ethanol. This increased surface area allows for enhanced contact between reactants and catalyst, promoting efficient conversion processes. Additionally, the optimal acidity of the H-USY catalyst, which is comparable to that of H–Y zeolite, plays a crucial role in promoting ethanol production pathways. The acidity of the catalyst facilitates the necessary chemical transformations involved in ethanol synthesis, such as the dehydration of intermediates and the formation of ethanol from WCPR.

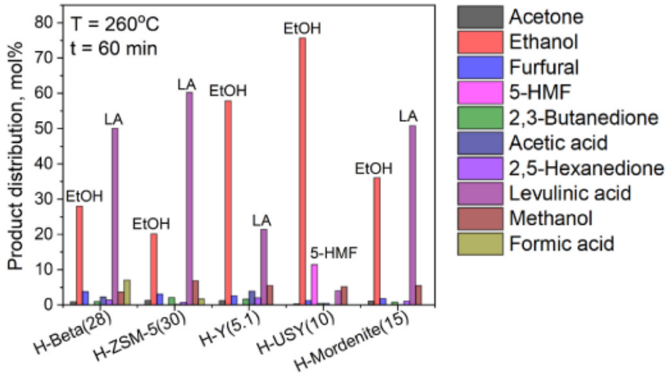

Fig. 8. The liquid-phase product distribution for the WT + Zeolite samples. Reaction conditions: 3.0 g of WCPR, 30 mL of water, 1.0 g of H-Beta, H-ZSM-5, H–Y, H-USY or H-Mordenite catalysts, stirring speed at 900 rpm, T = 260 °C, t = 60 min.

In the case of WT + Beta, WT + ZSM-5, and WT + Mordenite, the main product was LA, with the highest achieved selectivity of 60.2 % for the WT + ZSM-5, a trend consistent with observations at 220 °C. The ZSM-5 catalyst possesses several exceptional properties that may be directly related to its ability to yield high amounts of LA. Specifically, the ZSM-5 catalyst exhibits the highest number of Brønsted acid sites (BASs) among the studied catalysts, as indicated in Table S3. Additionally, the highest BAS/LAS ratio of 2.5 in H-ZSM-5, compared to other catalysts, suggests a favorable environment for the formation of LA. According to literature [46,47], BAS are known to play a crucial role in the rehydration of 5-HMF into LA and contribute to the cleavage of C–C bonds, which are key steps in the production of LA. The introduction of zeolite catalysts induces a noteworthy shift in product distribution. Notably, it enhances the formation of specific compounds, such as ethanol and LA, while reducing the presence of others like 5-HMF and

FUR, in comparison to the WT of WCPR without the presence of any catalyst. The catalyst is likely facilitating distinct reaction pathways, exerting a significant influence on the selectivity of product formation. In summary, the data strongly suggests that the product distribution in the WT of WCPR is intricately influenced by the presence of a catalyst, reaction time, and temperature.

3.7. Reaction pathways of WCPR into hydrochar and the liquid products in the presence of zeolite acid catalysts

WCPR subjected to WT with acid zeolite catalysts in a nitrogen atmosphere reveals intricate pathways leading to the production of LA and/or ethanol, illustrated in Fig. 9. The first process involves a sophisticated, multi-step sequence in the synthesis of LA from cellulose using H-ZSM-5 zeolite. In the initial step, cellulose undergoes hydrolysis, yielding glucose, which subsequently transforms into 5-HMF. Lewis's acid sites (LASs) of H-ZSM-5 catalyst play a crucial role in the dehydration of glucose, resulting in the creation of 5-HMF. Subsequent rehydration of 5-HMF into LA, the primary objective compound, is facilitated by Brønsted acid sites (BASs), contributing significantly to the cleavage of C–C bonds [48]. Notably, it is recognized [49,50] that, in acidic solutions, the direct dehydration of glucose into LA without the intermediate formation of fructose and 5-HMF is a plausible pathway. Simultaneously, glucose can undergo isomerization with LASs participation, leading to the production of fructose. Following this, fructose undergoes a dehydration reaction, giving rise to the formation of 5-HMF with the participation of BASs [46,47]. The subsequent rehydration of 5-HMF results in the production of LA and formic acid. Additionally, within the product mixture, furfural may be generated due to the liberation of formaldehyde from the 5-HMF compound [47,49]. The confirmed development of humins corresponds with established findings in the literature [51,52], indicating that in the presence of acid catalysis, the polymerization of glucose and 5-HMF has the potential to generate humins through aldol condensation, incorporating an intermediate compound identified as 2,5-dioxo-6-hydroxyhexanal.

The alternative parallel pathway unfolds through a series of distinct stages. Initiating the process is the hydrolysis of cellulose into glucose, catalyzed by the acid centers of H-USY zeolite, specifically LASs and BASs [46,53,54]. Subsequent to hydrolysis, glucose undergoes isomerization into fructose via LASs [55]. Following this, fructose sequentially transforms into hydroxyacetone through retro aldol-condensation. Ultimately, hydroxyacetone undergoes conversion into ethanol through the cleavage of C–C bonds. Simultaneously, acknowledgment is given to the plausible conversion of glucose into hydroxyacetone via retro aldol-condensation. Furthermore, it is posited that the direct conversion of cellulose into hydroxyacetone may occur, followed by the subsequent formation of ethanol through the C–C cleavage of hydroxyacetone. This route necessitates the activation and cleavage of specific C–C and C–O bonds. In contrast to recent literature [54–60], which has highlighted the direct production of ethanol from cellulose using different heterogeneous catalysts that involve the transformation of glycolaldehyde into ethylene glycol and promote the C–O cleavage of ethylene glycol to yield ethanol, a diverse range of reaction products has been revealed in this study. As a result, an alternative reaction mechanism is suggested, built upon the observed hydroxyacetone product. In addition to ethanol resulting from the C–C cleavage of hydroxyacetone, byproducts such as methanol and acetaldehyde were detected in the study. Furthermore, an additional quantity of ethanol can be obtained through acetaldehyde transfer hydrogenation, while acetic acid is produced through the oxidation of acetaldehyde. Finally, a minor amount of formaldehyde and CO_2 was detected, likely arising from the hydroxyacetone cracking process.

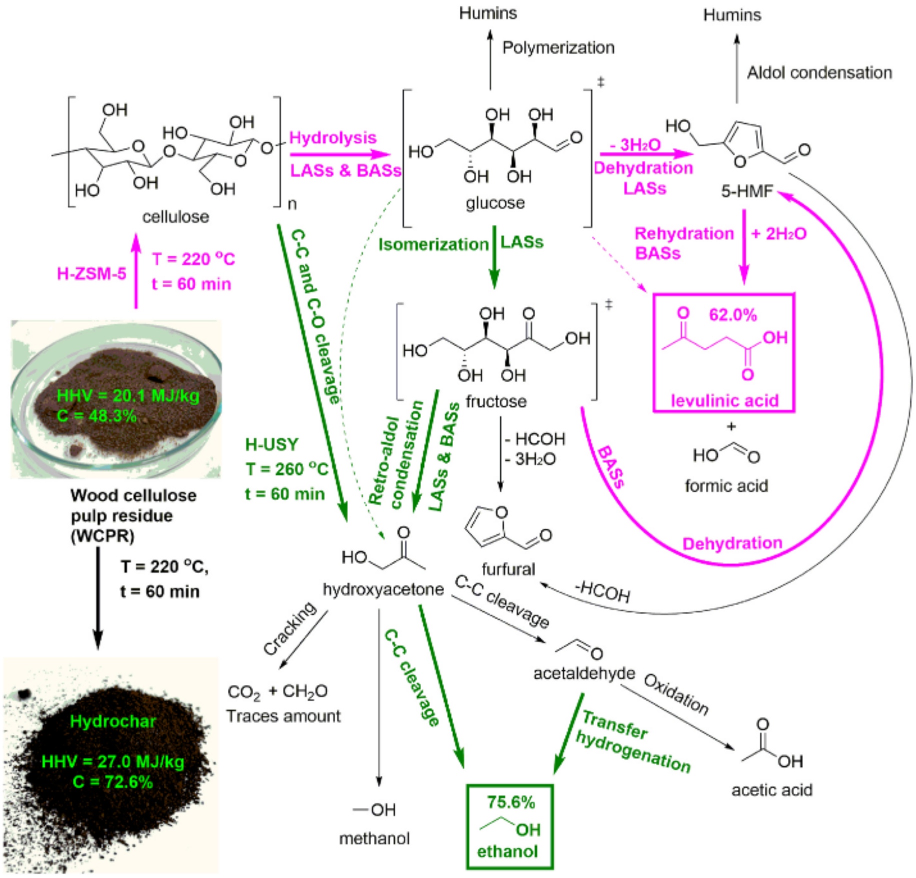

Fig. 9. Possible reaction pathway for the WT of WCPR with zeolite catalysts into hydrochar and the liquid value-added products.

4. Conclusions

The study introduces a novel approach for producing ethanol, levulinic acid (LA), and high-quality hydrochar from wood cellulose pulp residue (WCPR) via wet torrefaction (WT) facilitated by various zeolite acid catalysts. The aim was to comprehensively assess the influence of these catalysts and reaction conditions on hydrochar properties and liquid product distribution. Optimal conditions for bio-ethanol production were identified, with selectivity reaching 59.0 % at 220 °C for 15 min with the H–Y catalyst, while the highest bio-ethanol yield (75.6 %) was achieved using H-USY zeolite at 260 °C for 60 min. Notable LA production (62.0 %) occurred at 220 °C for 60 min, particularly with the H-ZSM-5 catalyst. Hydrochar properties were extensively evaluated, revealing significant carbon content (71.5 %) with WT + Mordenite (220 °C, 60 min), resulting in an HHV of 27.3 MJ/kg, an enhancement factor of 1.36, and a carbon enrichment factor of 1.48. The proposed reaction mechanism elucidates the conversion of cellulose into hydroxyacetone, followed by ethanol and LA production. This underscores WT's potential for biomass waste transformation into sustainable energy and valuable chemicals.

CRediT authorship contribution statement

Andrii Kostyniuk: Writing – review & editing, Writing – original draft, Visualization, Validation, Software, Project administration, Methodology, Investigation, Formal analysis, Data curation, Conceptualization. **Blaž Likozar:** Funding acquisition, Conceptualization, Methodology, Project administration, Resources, Supervision.

Declaration of competing interest

The authors declare that they have no known competing financial interests or personal relationships that could have appeared to influence the work reported in this paper.

Acknowledgements

The authors express their gratitude for the financial support provided by CARBIOW (Carbon Negative Biofuels from Organic Waste) project, which is funded by the European Commission and the European Climate, Infrastructure and Environment Executive Agency (CINEA) under the Horizon Europe Programme, under grant agreement ID: 101084443. The authors would also like to extend their thanks to Urška Kavčič for conducting N_2 physisorption measurements, Dr. Anže Prašnikar for performing SEM analysis, and Mr. Edi Kranjc for conducting XRD analysis. Additionally, they acknowledge the support received from BioTrainValue (BIOmass Valorisation via Superheated Steam Torrefaction, Pyrolysis, Gasification Amplified by Multidisciplinary Researchers TRAINing for Multiple Energy and Products' Added VALUEs), with project number: 101086411, funded under Horizon Europe's Maria Skłodowska-Curie Staff Exchange program.

Appendix A. Supplementary data

Supplementary data to this article can be found online at https://doi.org/10.1016/j.renene.2024.120509.

References

[1] Y. Wang, J.J. Wu, Thermochemical conversion of biomass: potential future prospects, Renew. Sustain. Energy Rev. 187 (2023) 113754, https://doi.org/10.1016/j.rser.2023.113754.
[2] Y. Li, Z. Tan, Y. Zhu, W. Zhang, Z. Du, J. Shao, L. Jiang, H. Yang, H. Chen, Effects of P-based additives on agricultural biomass torrefaction and particulate matter emissions from fuel combustion, Renew. Energy 190 (2022) 66–77, https://doi.org/10.1016/j.renene.2022.03.101.
[3] L. Jezerska, V. Sassmanova, R. Prokes, D. Gelnar, The pelletization and torrefaction of coffee grounds, garden chaff and rapeseed straw, Renew. Energy 210 (2023) 346–354, https://doi.org/10.1016/j.renene.2023.04.016.
[4] A. Sangjan, P. Ngamsiri, N. Klomkliang, K.C.W. Wu, B.M. Matsagar, S. Ratchahat, C.G. Liu, N. Laosiripojana, C. Sakdaronnarong, Effect of microwave-assisted wet torrefaction on liquefaction of biomass from palm oil and sugarcane wastes to bio-oil and carbon nanodots/nanoflakes by hydrothermolysis and solvothermolysis, Renew. Energy 154 (2020) 1204–1217, https://doi.org/10.1016/j.renene.2020.03.070.
[5] K.A. Abdulyekeen, A.A. Umar, M.F.A. Patah, W.M.A.W. Daud, Torrefaction of biomass: production of enhanced solid biofuel from municipal solid waste and other types of biomass, Renew. Sustain. Energy Rev. 150 (2021) 111436, https://doi.org/10.1016/j.rser.2021.111436.
[6] X. Zhu, Z. Luo, R. Diao, X. Zhu, Combining torrefaction pretreatment and co-pyrolysis to upgrade biochar derived from bio-oil distillation residue and walnut shell, Energy Convers. Manag. 199 (2019) 111970, https://doi.org/10.1016/j.enconman.2019.111970.
[7] A. Leontiev, B. Kichatov, A. Korshunov, A. Kiverin, V. Zaichenko, G. Sytchev, K. Melnikova, Oxidative torrefaction of pine pellets in the quiescent layer of mineral filler, Fuel Process. Technol. 182 (2018) 113–122, https://doi.org/10.1016/j.fuproc.2018.10.021.
[8] A. Iglesias Canabal, J. Proupín Castiñeiras, J.A. Rodríguez Añón, C. Eimil Fraga, R. Rodríguez Soalleiro, Predicting the energy properties of torrefied debarked pine pellets from torrefaction temperature and residence time, Renew. Energy 218 (2023) 119346, https://doi.org/10.1016/j.renene.2023.119346.
[9] R. Aguado, M. Cuevas, L. Pérez-Villarejo, M.L. Martínez-Cartas, S. Sánchez, Upgrading almond-tree pruning as a biofuel via wet torrefaction, Renew. Energy 145 (2020) 2091–2100, https://doi.org/10.1016/j.renene.2019.07.142.
[10] Q.V. Bach, W.H. Chen, S.C. Lin, H.K. Sheen, J.S. Chang, Wet torrefaction of microalga Chlorella vulgaris ESP-31 with microwave-assisted heating, Energy Convers. Manag. 141 (2017) 163–170, https://doi.org/10.1016/j.enconman.2016.07.035.
[11] M. Alam, D. Rammohan, N.R. Peela, Catalytic co-pyrolysis of wet-torrefied bamboo sawdust and plastic over the zeolite H-ZSM-5: Synergistic effects and kinetics, Renew. Energy 178 (2021) 608–619, https://doi.org/10.1016/j.renene.2021.06.109.
[12] A. Kostyniuk, B. Likozar, Wet torrefaction of biomass waste into value-added liquid product (5-HMF) and high quality solid fuel (hydrochar) in a nitrogen atmosphere, Renew. Energy. 226 (2024) 120450, https://doi.org/10.1016/j.renene.2024.120450.
[13] Statista Research Department, Production of Wood Pulp Worldwide from 1961 to 2022, 2023. https://www.statista.com/statistics/240570/consumption-and-production-of-fibrous-material-worldwide/.
[14] A. Kostyniuk, B. Likozar, Catalytic wet torrefaction of biomass waste into bio-ethanol, levulinic acid, and high quality solid fuel, Chem. Eng. J. 485 (2024) 149779.
[15] A. Kostyniuk, B. Likozar, Wet torrefaction of biomass waste into levulinic acid and high-quality hydrochar using H-beta zeolite catalyst, J. Clean. Prod. 449 (2024) 141735, https://doi.org/10.1016/j.jclepro.2024.141735.
[16] A. Kostyniuk, D. Bajec, P. Djinović, B. Likozar, Allyl alcohol production by gas phase conversion reactions of glycerol over bifunctional hierarchical zeolite-supported bi- and tri-metallic catalysts, Chem. Eng. J. 397 (2020) 125430, https://doi.org/10.1016/j.cej.2020.125430.
[17] A. Kostyniuk, D. Bajec, A. Prašnikar, B. Likozar, Catalytic hydrocracking, hydrogenation, and isomerization reactions of model biomass tar over (W/Ni)-zeolites, J. Ind. Eng. Chem. 101 (2021) 293–306, https://doi.org/10.1016/j.jiec.2021.06.001.
[18] A. Kostyniuk, D. Bajec, B. Likozar, Catalytic hydrocracking reactions of tetralin biomass tar model compound to benzene, toluene and xylenes (BTX) over metal-modified ZSM-5 in ambient pressure reactor, Renew. Energy 188 (2022) 240–255, https://doi.org/10.1016/j.renene.2022.01.090.
[19] A. Kostyniuk, D. Bajec, B. Likozar, Catalytic hydrocracking reactions of tetralin as aromatic biomass tar model compound to benzene/toluene/xylenes (BTX) over zeolites under ambient pressure conditions, J. Ind. Eng. Chem. 96 (2021) 130–143, https://doi.org/10.1016/j.jiec.2021.01.010.
[20] A. Kostyniuk, D. Bajec, P. Djinović, B. Likozar, One-step synthesis of glycidol from glycerol in a gas-phase packed-bed continuous flow reactor over HZSM-5 zeolite catalysts modified by CsNO3, Chem. Eng. J. 394 (2020) 124945, https://doi.org/10.1016/j.cej.2020.124945.
[21] R. García, C. Pizarro, A.G. Lavín, J.L. Bueno, Biomass proximate analysis using thermogravimetry, Bioresour. Technol. 139 (2013) 1–4, https://doi.org/10.1016/j.biortech.2013.03.197.
[22] X. Li, Z. Lu, J. Chen, X. Chen, Y. Jiang, J. Jian, S. Yao, Effect of oxidative torrefaction on high temperature combustion process of wood sphere, Fuel 286 (2021) 119379, https://doi.org/10.1016/j.fuel.2020.119379.
[23] R. García, C. Pizarro, A.G. Lavín, J.L. Bueno, Characterization of Spanish biomass wastes for energy use, Bioresour. Technol. 103 (2012) 249–258, https://doi.org/10.1016/j.biortech.2011.10.004.
[24] X. Niu, Y. Xu, L. Shen, Effect of torrefaction on the evolution of carbon and nitrogen during chemical looping gasification of rapeseed cake, Chem. Eng. J. 450 (2022) 138134, https://doi.org/10.1016/j.cej.2022.138134.
[25] Y. Wang, X. Zhu, S. Li, Y. Song, G. Chen, L. Hou, Wet torrefaction coupled pyrolysis of camel dung: fuel properties, pyrolysis behaviors and evolved gases, Fuel 352 (2023) 129026, https://doi.org/10.1016/j.fuel.2023.129026.
[26] D. Chen, A. Gao, K. Cen, J. Zhang, X. Cao, Z. Ma, Investigation of biomass torrefaction based on three major components: hemicellulose, cellulose, and lignin,

Energy Convers. Manag. 169 (2018) 228–237, https://doi.org/10.1016/j.enconman.2018.05.063.

[27] C. Zhang, S.H. Ho, W.H. Chen, Y. Xie, Z. Liu, J.S. Chang, Torrefaction performance and energy usage of biomass wastes and their correlations with torrefaction severity index, Appl. Energy 220 (2018) 598–604, https://doi.org/10.1016/j.apenergy.2018.03.129.

[28] M.F. Li, Y. Shen, J.K. Sun, J. Bian, C.Z. Chen, R.C. Sun, Wet torrefaction of bamboo in Hydrochloric acid solution by microwave heating, ACS Sustain. Chem. Eng. 3 (2015) 2022–2029, https://doi.org/10.1021/acssuschemeng.5b00296.

[29] A. Aranzabal, J.A. González-Marcos, M. Romero-Sáez, J.R. González-Velasco, M. Guillemot, P. Magnoux, Stability of protonic zeolites in the catalytic oxidation of chlorinated VOCs (1,2-dichloroethane), Appl. Catal. B Environ. 88 (2009) 533–541, https://doi.org/10.1016/j.apcatb.2008.10.007.

[30] M. Wilk, M. Śliz, K. Czerwińska, M. Śledź, The effect of an acid catalyst on the hydrothermal carbonization of sewage sludge, J. Environ. Manage. 345 (2023), https://doi.org/10.1016/j.jenvman.2023.118820.

[31] M. Ameen, N.M. Zamri, S.T. May, M.T. Azizan, A. Aqsha, N. Sabzoi, F. Sher, Effect of acid catalysts on hydrothermal carbonization of Malaysian oil palm residues (leaves, fronds, and shells) for hydrochar production, Biomass Convers. Biorefinery 12 (2022) 103–114, https://doi.org/10.1007/s13399-020-01201-2.

[32] C. He, C. Tang, C. Li, J. Yuan, K.Q. Tran, Q.V. Bach, R. Qiu, Y. Yang, Wet torrefaction of biomass for high quality solid fuel production: a review, Renew. Sustain. Energy Rev. 91 (2018) 259–271, https://doi.org/10.1016/j.rser.2018.03.097.

[33] D. Chen, K. Cen, F. Chen, Y. Zhang, Solar pyrolysis of cotton stalks: combined effects of torrefaction pretreatment and HZSM-5 zeolite on the bio-fuels upgradation, Energy Convers. Manag. 261 (2022) 115640, https://doi.org/10.1016/j.enconman.2022.115640.

[34] L. Dai, C. He, Y. Wang, Y. Liu, Z. Yu, Y. Zhou, L. Fan, D. Duan, R. Ruan, Comparative study on microwave and conventional hydrothermal pretreatment of bamboo sawdust: hydrochar properties and its pyrolysis behaviors, Energy Convers. Manag. 146 (2017) 1–7, https://doi.org/10.1016/j.enconman.2017.05.007.

[35] Y. Wang, Q. Wu, L. Dai, Z. Zeng, Y. Liu, R. Ruan, G. Fu, Z. Yu, L. Jiang, Co-pyrolysis of wet torrefied bamboo sawdust and soapstock, J. Anal. Appl. Pyrolysis 132 (2018) 211–216, https://doi.org/10.1016/j.jaap.2018.02.012.

[36] S. Zhang, T. Chen, Y. Xiong, Q. Dong, Effects of wet torrefaction on the physicochemical properties and pyrolysis product properties of rice husk, Energy Convers. Manag. 141 (2017) 403–409, https://doi.org/10.1016/j.enconman.2016.10.002.

[37] X. Wang, J. Wu, Y. Chen, A. Pattiya, H. Yang, H. Chen, Comparative study of wet and dry torrefaction of corn stalk and the effect on biomass pyrolysis polygeneration, Bioresour. Technol. 258 (2018) 88–97, https://doi.org/10.1016/j.biortech.2018.02.114.

[38] J. Jian, Z. Lu, S. Yao, X. Li, W. Song, Comparative study on pyrolysis of wet and dry torrefied beech wood and wheat straw, Energy Fuel. 33 (2019) 3267–3274, https://doi.org/10.1021/acs.energyfuels.8b04501.

[39] Q. Ma, L. Han, G. Huang, Effect of water-washing of wheat straw and hydrothermal temperature on its hydrochar evolution and combustion properties, Bioresour. Technol. 269 (2018) 96–103, https://doi.org/10.1016/j.biortech.2018.08.082.

[40] Q.V. Bach, K.Q. Tran, Ø. Skreiberg, T.T. Trinh, Effects of wet torrefaction on pyrolysis of woody biomass fuels, Energy 88 (2015) 443–456, https://doi.org/10.1016/j.energy.2015.05.062.

[41] M. Volpe, L. Fiori, From olive waste to solid biofuel through hydrothermal carbonisation: the role of temperature and solid load on secondary char formation and hydrochar energy properties, J. Anal. Appl. Pyrolysis 124 (2017) 63–72, https://doi.org/10.1016/j.jaap.2017.02.022.

[42] P. Gao, Y. Zhou, F. Meng, Y. Zhang, Z. Liu, W. Zhang, G. Xue, Preparation and characterization of hydrochar from waste eucalyptus bark by hydrothermal carbonization, Energy 97 (2016) 238–245, https://doi.org/10.1016/j.energy.2015.12.123.

[43] G.K. Parshetti, S. Kent Hoekman, R. Balasubramanian, Chemical, structural and combustion characteristics of carbonaceous products obtained by hydrothermal carbonization of palm empty fruit bunches, Bioresour. Technol. 135 (2013) 683–689, https://doi.org/10.1016/j.biortech.2012.09.042.

[44] M. Pala, I.C. Kantarli, H.B. Buyukisik, J. Yanik, Hydrothermal carbonization and torrefaction of grape pomace: a comparative evaluation, Bioresour. Technol. 161 (2014) 255–262, https://doi.org/10.1016/j.biortech.2014.03.052.

[45] A. Missaoui, S. Bostyn, V. Belandria, B. Cagnon, B. Sarh, I. Gökalp, Hydrothermal carbonization of dried olive pomace: energy potential and process performances, J. Anal. Appl. Pyrolysis 128 (2017) 281–290, https://doi.org/10.1016/j.jaap.2017.09.022.

[46] C. Ma, B. Cai, L. Zhang, J. Feng, H. Pan, Acid-catalyzed conversion of cellulose into levulinic acid with Biphasic solvent system, Front. Plant Sci. 12 (2021), https://doi.org/10.3389/fpls.2021.630807.

[47] N.A.S. Ramli, N.A.S. Amin, Optimization of renewable levulinic acid production from glucose conversion catalyzed by Fe/HY zeolite catalyst in aqueous medium, Energy Convers. Manag. 95 (2015) 10–19, https://doi.org/10.1016/j.enconman.2015.02.013.

[48] X. Li, R. Xu, J. Yang, S. Nie, D. Liu, Y. Liu, C. Si, Production of 5-hydroxymethylfurfural and levulinic acid from lignocellulosic biomass and catalytic upgradation, Ind. Crops Prod. 130 (2019) 184–197, https://doi.org/10.1016/j.indcrop.2018.12.082.

[49] G. Yang, E.A. Pidko, E.J.M. Hensen, Mechanism of Bronsted acid-catalyzed conversion of carbohydrates, J. Catal. 295 (2012) 122–132, https://doi.org/10.1016/j.jcat.2012.08.002.

[50] Z. Sun, L. Xue, S. Wang, X. Wang, J. Shi, Single step conversion of cellulose to levulinic acid using temperature-responsive dodeca-aluminotungstic acid catalysts, Green Chem. 18 (2016) 742–752, https://doi.org/10.1039/c5gc01730k.

[51] S.S. Chen, I.K.M. Yu, D.C.W. Tsang, A.C.K. Yip, E. Khan, L. Wang, Y.S. Ok, C. S. Poon, Valorization of cellulosic food waste into levulinic acid catalyzed by heterogeneous BrØnsted acids: temperature and solvent effects, Chem. Eng. J. 327 (2017) 328–335, https://doi.org/10.1016/j.cej.2017.06.108.

[52] M. Mikola, J. Ahola, J. Tanskanen, Production of levulinic acid from glucose in sulfolane/water mixtures, Chem. Eng. Res. Des. 148 (2019) 291–297, https://doi.org/10.1016/j.cherd.2019.06.022.

[53] N. Karanwal, R.G. Kurniawan, J. Park, D. Verma, S. Oh, S.M. Kim, S.K. Kwak, J. Kim, One-pot, cascade conversion of cellulose to γ-valerolactone over a multifunctional Ru–Cu/zeolite-Y catalyst in supercritical methanol, Appl. Catal. B Environ. 314 (2022) 121466, https://doi.org/10.1016/j.apcatb.2022.121466.

[54] Z. Su, J. Zhang, S. Lu, F.S. Xiao, Pt nanoparticles supported on Nb-modified TiO2 as an efficient heterogeneous catalyst for the conversion of cellulose to light bioalcohols, Chem. Commun. 58 (2022) 12349–12352, https://doi.org/10.1039/d2cc03845e.

[55] H. Song, P. Wang, S. Li, W. Deng, Y. Li, Q. Zhang, Y. Wang, Direct conversion of cellulose into ethanol catalysed by a combination of tungstic acid and zirconia-supported Pt nanoparticles, Chem. Commun. 55 (2019) 4303–4306, https://doi.org/10.1039/c9cc00619b.

[56] C. Li, G. Xu, C. Wang, L. Ma, Y. Qiao, Y. Zhang, Y. Fu, One-pot chemocatalytic transformation of cellulose to ethanol over Ru-WOx/HZSM-5, Green Chem. 21 (2019) 2234–2239, https://doi.org/10.1039/c9gc00719a.

[57] M. Yang, H. Qi, F. Liu, Y. Ren, X. Pan, L. Zhang, X. Liu, H. Wang, J. Pang, M. Zheng, A. Wang, T. Zhang, One-pot production of cellulosic ethanol via Tandem catalysis over a multifunctional Mo/Pt/WOx catalyst, Joule 3 (2019) 1937–1948, https://doi.org/10.1016/j.joule.2019.05.020.

[58] Y. Wu, C. Dong, H. Wang, J. Peng, Y. Li, C. Samart, M. Ding, One-pot ethanol production from cellulose transformation over multifunctional Pt/WOx and Hollow Pt@HZSM-5 catalysts, ACS Sustain. Chem. Eng. 10 (2022) 2802–2810, https://doi.org/10.1021/acssuschemeng.1c08204.

[59] Q. Liu, H. Wang, H. Xin, C. Wang, L. Yan, Y. Wang, Q. Zhang, X. Zhang, Y. Xu, G. W. Huber, L. Ma, Selective cellulose hydrogenolysis to ethanol using Ni@C combined with phosphoric acid catalysts, ChemSusChem 12 (2019) 3977–3987, https://doi.org/10.1002/cssc.201901110.

[60] D. Chu, Y. Xin, C. Zhao, Production of bio-ethanol by consecutive hydrogenolysis of corn-stalk cellulose, Chinese J. Catal. 42 (2021) 844–854, https://doi.org/10.1016/S1872-2067(20)63709-3.